Title

Numerical and Experimental Investigation of Heat Transfer in the Porous Media of an Additively Manufactured Evaporator of a Two-Phase Mechanically Pumped Loop for Space Applications

Permalink

https://escholarship.org/uc/item/2rp3c997

Journal

Microgravity Science and Technology, 36(4)

ISSN

0938-0108

Authors

Valdarno, Luca
Dhir, Vijay K
Furst, Benjamin
et al.

Publication Date

2024

DOI

10.1007/s12217-024-10122-y

Peer reviewed

Microgravity Science and Technology (2024) 36:40
https://doi.org/10.1007/s12217-024-10122-y

RESEARCH

Numerical and Experimental Investigation of Heat Transfer in the Porous Media of an Additively Manufactured Evaporator of a Two-Phase Mechanically Pumped Loop for Space Applications

Luca Valdarno[1,2] · **Vijay K. Dhir**[1] · **Benjamin Furst**[2] · **Eric Sunada**[2]

Received: 18 August 2023 / Accepted: 20 May 2024 / Published online: 29 June 2024

Abstract

Two-phase pumped cooling systems are applied when it is required to maintain a very stable temperature for heat dissipation in a system. A novel additively manufactured evaporator for two-phase thermal control was developed at NASA Jet Propulsion Laboratory (JPL). The Two-Phase Mechanically Pumped Loop (2PMPL) allows to manage the heat transfer with much wider breadth of control authority compared to capillary-based systems, while alleviating the system's sensitivity to pressure drops. The focus of this work is the understanding and capturing the micro-scale evaporation occurring in the porous structure of the evaporator. The Boiling and Phase Change Heat Transfer Laboratory at the University of California, Los Angeles (UCLA) developed an all-encompassing numerical simulation tool to predict the operational thermal behavior of the evaporator considering the effect of the liquid-vapor interface at the wick-to-vapor boundary. The numerical model incorporated the behaviour of the liquid-vapor meniscus at particle level located along the evaporative boundary between the wick structure and the vapor chamber. The numerical model allowed to study the effect of different parameters, such as boundary conditions, geometry, wick and fluid properties. An experimental setup was built at UCLA in order to characterize the heat transfer within an additively manufactured porous sample fabricated at JPL and in particular its evaporative heat load under certain heat inputs. The experimental efforts served as validation for the numerical results and aided in the characterization of the transient phenomena, such as dry-out.

Keywords Porous media · Two-phase evaporator · Mechanically pumped loop · Additive manufacturing

Introduction

Two-phase pumped loops systems are listed in NASA's technology road-map as an enabling thermal control technology for space applications. While Heat Pipe (HP), Capillary Pumped Loop (CPL) and Loop Heat Pipe (LHP) have achieved a high Technology Readiness Level (TRL) by providing major benefits over the traditional thermal management approach, these technologies alone will not be able to support the requirements of all future scientific spacecrafts (Sargusingh et al. 2018). Sunada et al. (2016) described how the Two-Phase Mechanically Pumped Loop (2PMPL) could enable new deep space science missions as a novel thermal management technology.

The 2PMPL developed at JPL is very similar to a CPL since it separates the fluid phases in the evaporator but it can count on the addition of a centrifugal pump and a by-pass line that connects the outlet of the pump to the condenser outlet. Figure 1 illustrates the basic concept of the 2PMPL. The mechanical pump and the by-pass line assist the fluid flow in addition to the capillary pumping and allow to control the pressure at condenser outlet. Reduced pressure at the condenser outlet provides a suction head that assists the capillary forces in moving the fluid through the evaporator. These two elements significantly impact the performance of the fluid loop and enable the thermal management of much larger systems subjected to higher heat loads.

During the operational nominal conditions, a constant heat load is applied to the evaporator, the pump operates at constant speed and the accumulator temperature is held constant.

✉ Vijay K. Dhir
vdhir@seas.ucla.edu

[1] Department of Mechanical and Aerospace Engineering, University of California, Los Angeles 90095, CA, US

[2] Jet Propulsion Laboratory / California Institute of Technology, Pasadena 91109, CA, US

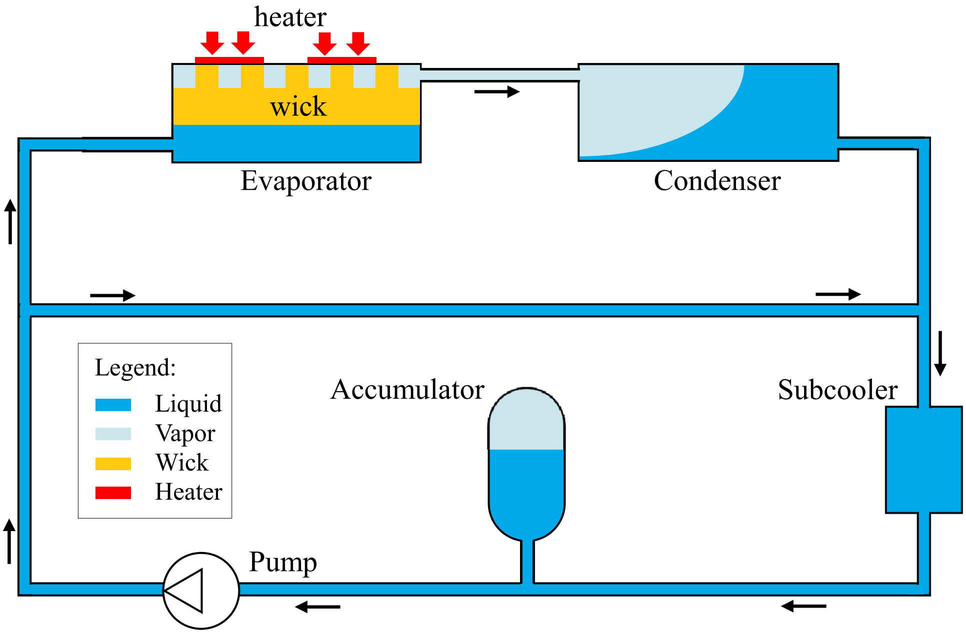

Fig. 1 JPL Two-Phase Mechanically Pumped Loop layout

The pressure loss in the by-pass line depends on the flow rate dictated by the pump and the by-pass fluid resistance. The pressure in the vapor grooves is higher than the pressure in the liquid chamber preventing the liquid from invading the vapor grooves due to the action of the pump. In both the liquid and vapor lines at the inlet and outlet of the evaporator, pressure decreases monotonically due to the fluid flow.

The flexibility of the 2PMPL lies in the capability to reclaim waste heat dissipation, to reject heat from discrete locations (multiple evaporators and condensers) and to control the loop temperature with minimal power. Another key aspect of this technology is the ability to integrate multiphase heat transfer provisions directly with structural elements thanks to the conjunct use of the Additive Manufacturing (AM) Technology. In the event of pump failure, the system could operate as a CPL at lower performance.

Evaporator Layout

In the evaporator heat from the payload is absorbed promoting the liquid-to-vapor phase change. The evaporator contains two channels separated by a porous wick, as shown in Fig. 2. The wick serves as a phase separator and ensures that only vapor exits through the vapor line. Thereafter the vapor flows to a condenser where it condenses back into liquid, and combines with the liquid exiting the by-pass line.

The evaporator chamber has a rectangular cross-section that is split into two chambers (liquid and vapor) by a porous plate that serves as wick. Vapor occupies the upper chamber thus formed, whereas subcooled liquid flows in the lower chamber. The upper plate of the evaporator is subjected to uniform heat input. Several porous pillars serve to transport heat from the top plate to the upper surface of the wick. Liquid in the lower chamber needs to remain subcooled to reduce any chances of vapor formation in the liquid chamber. Similarly, pressure in the vapor chamber (capillary pressure) needs to remain sufficiently high to eliminate migration of liquid into the vapor chamber. Vapor generated as a result of evaporation at the wick interface occupies the vapor chamber and creates a nearly isothermal condition on the back side of the heat receiving surface. Vapor is also superheated as a result of heat transfer from the upper chamber walls and the pillar transferring heat to the wick. Vapor exiting the chamber is converted into liquid in the condenser.

As summarized in Table 1, the baseline evaporator unit measures 213 x 198 x 16 mm^3 and has a mass of 1.3 kg. The wick material, separating the liquid channel from the vapor grooves, is additively manufactured along with the rest of the evaporator. The maximum pore radius is 18 µm with an average value of 6 µm. The measured permeability is 3.2 x 10^{-13} m^2 and porosity is 22.3%. The baseline design presents a wick thickness of 4 mm and a pillar 1 x 1 x 10 mm. The distance between two consecutive pillars (vapor groove) is 1 mm. Two main heaters are placed on top of the evaporator on a surface of 50.8 x 101.6 mm providing a power of 250 W each maximum (4.8 W cm^{-2}).

The fluid selected for the 2PMPL is ammonia at 10.34 bar (fluid properties are reported in Table 2). At the operating temperature of unmanned spacecraft missions, ammonia has the most favorable thermodynamic properties. The highest performance is obtained by utilizing a working fluid that has low freezing temperature, high surface tension, high latent heat, and low liquid viscosity. This selection is a result of a trade-off between many criteria such as: heat transport performance, chemical compatibility, mass of the system, power consumption of the pump, accumulator sizing, tubing, etc.

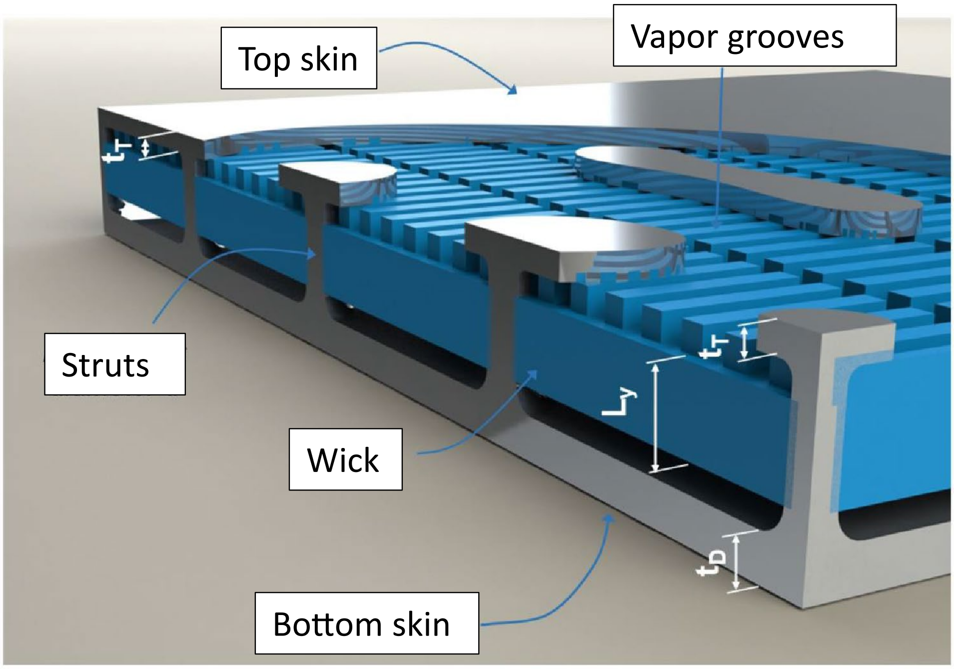

Fig. 2 Evaporator layout

In a nominal operational case, where the liquid-vapor interface is located along the boundary between wick and vapor grooves, the majority of heat transfer takes place along the liquid-vapor interface of the menisci in the form of evaporation. The vapor channels aid the development of the evaporating surface and the removal of the vapor that flows into the vapor line to move towards the condenser. The liquid-vapor interface adjusts itself to steady conditions at various heat fluxes by spontaneously changing the curvature of the menisci and the location in the porous media. Test results show that the evaporator unit can keep spatial isothermality within 0.5 °C for heat loads up to 100 W and within 3 °C for heat loads up to 325 W (Furst et al. 2018).

Figus et al. (1999) developed a pore network model to account for the distribution of pore sizes within the porous structure. This modeling approach represents the pore space through a network comprising sites (pores) and connections (throats). Additionally, a supplementary network is incorporated to factor in conductive heat transfer. The authors hypothesize the existence of an initial vapor zone within the wick, instigating the onset of vapor expansion.

In this study, a comprehensive model was developed to focus on the heat and mass transfer occurring within the wick structure and at the interface boundary during an operational steady-state regime. The accuracy of the model was verified through comparison with experimental data obtained from a specially designed experiment.

Table 1 Main features of the ammonia evaporator (Furst et al. 2018)

Housing	Area [mm^2]	213 x 197
	Thickness [mm]	16
Porous Structure	Thickness [mm]	4
	Max. pore radius [µm]	18
	Porosity [%]	22.3
	Permeability [m^2]	3.2 x 10^{-13}
Vapor grooves	Size [mm^3]	1 x 1 x 10
	Pitch [mm]	1

Mathematical Model

Wick Model

A porous structure with heating and evaporation on the upper surface is shown in Fig. 3. The wick domain is fully saturated with liquid that flows to the liquid-vapor interface

Table 2 Thermal properties of ammonia NH_3 at 10.34 bar (Lemmon et al. 2018)

Property	Unit	Value
Boiling point	°C	26
Density	kg m^{-3}	601.45
Dynamic viscosity	Pa s	0.00012604
Specific heat	J kg^{-1} K^{-1}	4788.8
Heat of vaporization	J kg^{-1}	1161.6
Surface tension	N m^{-1}	0.02028
Thermal conductivity	W m^{-1} K^{-1}	0.468
Molar mass	g mol^{-1}	17.03

where evaporation takes place. Heat is applied on the external surface of the evaporator and is transferred to the wick pillar and then towards the liquid-vapor interface located at the wick-to-vapor groove boundary. This model is valid for an operational mode of the evaporator where the wick is fully saturated with liquid at thermal steady-state. Bubbles do not form within the wick unless the temperature differential between the maximum temperature and the saturation temperature exceeds the threshold for nucleation superheat.

Assumptions

The following assumptions are made:

1. Thermal steady-state, valid for operational cases where no transient phenomena, such as nucleation and boiling, take place.
2. Wick structure fully saturated with liquid, valid for low or moderate heat loads where the interface vapor-liquid is located at the surface of the wick.
3. Homogeneous and isotropic porous structure.
4. Negligible gravitational effects.
5. Newtonian fluid and constant thermal properties, valid for typical working fluids used for two-phase technologies and within a specific range of temperatures.
6. Zero thickness of the liquid-vapor interface. The liquid and vapor thermal properties change across this interface.
7. Temperature at the liquid-vapor interface is the saturation temperature at the local static pressure.

Mathematical Formulation

The wick structure in the evaporator can be represented by a two-dimensional elementary cell due to geometrical and physical symmetry. During nominal operation, the wick domain is fully saturated with liquid and the liquid-vapor interface is located at the boundary between the vapor groove and the wick. The fluid flow in the wick is determined based on continuity, Darcy and advection-diffusion equations. Evaporation occurs along the top interface with variable intensity, increasing in proximity of the heat source. The heat transfer is a result of the combination of evaporation, heat conduction within the porous media and convection of the cooling working liquid.

Figure 3 illustrates the wick structure domain Ω composed of a porous base with L_x width and L_y thickness and a porous pillar with L_{xp} width and L_{yp} height. The origin of the global coordinate system (x, y) is located at the bottom left corner of the domain.

Heat is applied uniformly on the top edge of the pillar, while evaporation takes place along the interface between the wick and the vapor groove. The side walls are adiabatic and impermeable (symmetry condition). The liquid flows throughout the wick domain from the bottom boundary, where the liquid chamber is located, up to the liquid-vapor interface due to capillary action. In order to sustain the liquid flow to compensate for evaporation, the capillary pressure must be equal to the sum of all other pressure drops.

This configuration represents the nominal case in which the wick structure operates far from the incipience

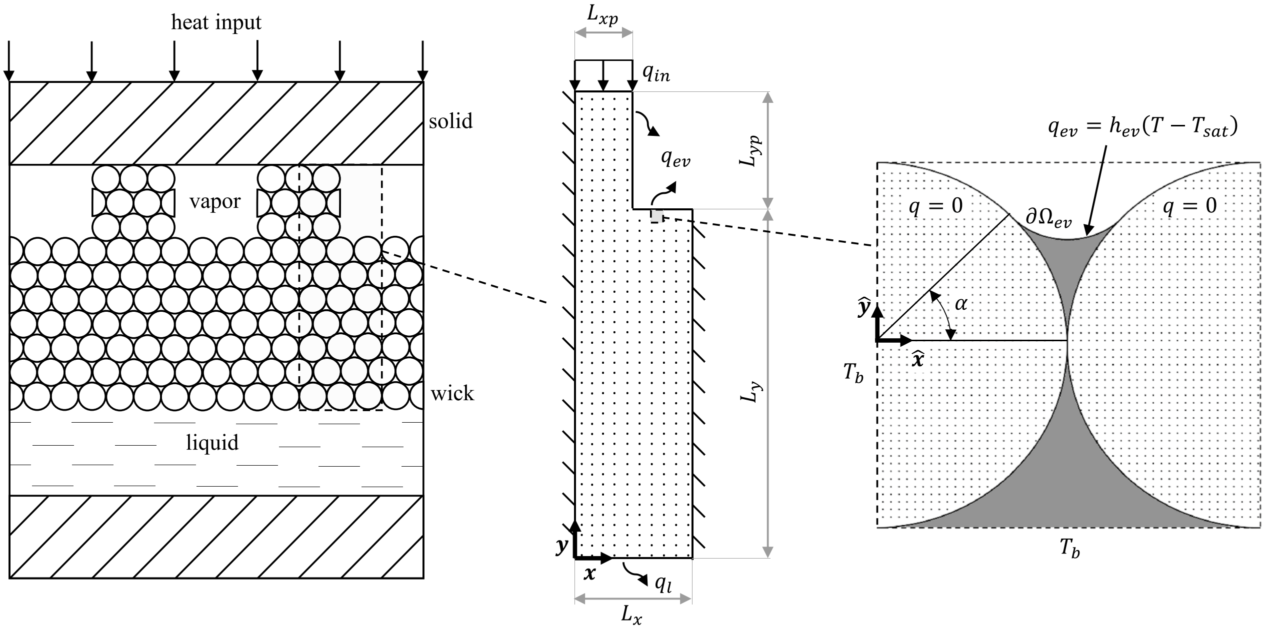

Fig. 3 Schematic of the evaporator cross-section (left). Elementary cell / wick model (center). Particle model (right)

of boiling. Bubble formation does not occur in the porous domain if the difference between the maximum temperature and the saturation temperature is less than the superheat for onset of nucleation. In the event this condition is not met, vapor would be generated within the domain resulting in an increase in thermal resistance and decrease in efficiency of evaporation at the liquid-vapor-solid interface. The liquid flow in the porous structure can be described by the continuity equation:

$$\frac{\partial u}{\partial x} + \frac{\partial v}{\partial y} = 0 \tag{1}$$

where u and v are respectively the fluid velocity components along x and y axes. This equation is coupled with the Darcy's law with gravity neglected:

$$\begin{cases} u = \frac{K}{\mu}\left(-\frac{\partial P}{\partial x}\right) \\ v = \frac{K}{\mu}\left(-\frac{\partial P}{\partial y}\right) \end{cases} \tag{2}$$

where P is the pressure variable, μ is the dynamic viscosity, K is the wick permeability that is determined by particle packing, sorting and particle size according to the Carman-Kozeny correlation (Carman 1937):

$$K = r_{part}^2 \frac{\epsilon^3}{37.5(1-\epsilon)^2} \tag{3}$$

where r_{part} is the particle radius and ϵ the porosity. The above relationship is valid for unconsolidated packed, spherical particles, plain or sintered, with a diameter spanning between 50 and 300 µm, and porosity between 27 and 66%. The particle radius is assumed to be four times the pore radius due to geometrical considerations valid for spherical particles. The energy equation, where T is the temperature variable, is

$$u\frac{\partial T}{\partial x} + v\frac{\partial T}{\partial y} = \alpha_e\left(\frac{\partial^2 T}{\partial x^2} + \frac{\partial^2 T}{\partial y^2}\right) \tag{4}$$

where the effective thermal diffusivity α_e is defined as,

$$\alpha_e = \frac{k_e}{\rho_l c_p} \tag{5}$$

where ρ_l is the liquid density, c_p is the specific heat, and the effective thermal conductivity k_e is calculated as,

$$k_e = \frac{k_s\left(2k_s + k_l - 2\epsilon\left(k_s - k_l\right)\right)}{2k_s + k_l + \epsilon(k_s - k_l)} \tag{6}$$

where k_s and k_l are respectively the thermal conductivities of the solid and liquid phases. It is valid for sintered metal powder wicks and it was confirmed experimentally by Gorring and Churchill (1961). The boundary conditions can be expressed at the heat input, convective and adiabatic borders respectively as,

$$\begin{cases} -k_e\frac{\partial T}{\partial y} = q_{in} & \text{for } y = L_y + L_{yp} \text{ and } x \in [0, L_{xp}] \\ -k_e\frac{\partial T}{\partial y} = h_l(T - T_l) & \text{for } y = 0 \\ \frac{\partial T}{\partial x} = 0 & \text{for } x = 0 \text{ and } x = L_x \end{cases} \tag{7}$$

and

$$\begin{cases} \frac{\partial P}{\partial y} = 0 \ \text{ for } y = L_y + L_{yp} \text{ and } x \in [0, L_{xp}] \\ P = P_l \ \text{ for } y = 0 \\ \frac{\partial P}{\partial x} = 0 \ \text{ for } x = 0 \text{ and } x = L_x \end{cases} \tag{8}$$

where T_l and P_l are respectively the temperature and pressure of the liquid chamber, q_{in} is the imposed heat flux and h_l is the convective heat transfer coefficient at the bottom liquid boundary calculated from the Nusselt number Nu as function of the Reynolds Re and Prandtl Pr numbers

$$Nu = \frac{h_l L}{k_l} = 7.54 + \frac{0.03\left(\frac{D_h}{L}RePr\right)}{1 + 0.016\left[\left(\frac{D_h}{L}\right)RePr\right]^{\frac{2}{3}}} \tag{9}$$

where k_l is the fluid thermal conductivity, D_h is the hydraulic diameter and L is the length of the chamber. This relationship is valid for laminar flow ($Re < 2800$) between isothermal parallel plates (Faghri 1995).

The boundary conditions along the evaporative boundary Ω_{ev} are calculated considering the mass balance and the Darcy flow equation,

$$\mathbf{q_{ev}} = -k_e \nabla T|_{\partial\Omega_{ev}} = \dot{\mathbf{m}}_\mathbf{l} h_{fg} = \rho_l \mathbf{v_l} h_{fg} = \rho_l\left(-\frac{K}{\mu}\nabla P|_{\partial\Omega_{ev}}\right)h_{fg} \tag{10}$$

where h_{fg} is the latent heat, $\mathbf{q_{ev}}$, $\mathbf{v_l}$ and $\dot{\mathbf{m}}_\mathbf{l}$ are respectively the evaporative heat flux, liquid velocity and mass flow rate vectors parallel to the x and y axes along the evaporative boundary. This equation becomes a boundary condition for the pressure field

$$\nabla P|_{\partial\Omega_{ev}} = \frac{k_e}{K}\frac{\mu}{\rho_l h_{fg}}\nabla T|_{\partial\Omega_{ev}} \tag{11}$$

and the boundary condition for the temperature field is

$$-k_e \nabla T|_{\partial\Omega_{ev}} = h_{ev}(T - T_{sat}) \tag{12}$$

where T_{sat} is the saturation temperature and h_{ev} is the evaporative heat transfer coefficient, calculated directly from the kinetic theory. It is a function of the fluid properties at a given pressure:

$$h_{ev} = \left(\frac{2\hat{a}}{2-\hat{a}}\right)\left(\frac{\widetilde{M}}{2\pi\widetilde{R}T_{sat}}\right)^{\frac{1}{2}}\rho_v\frac{h_{fg}^2}{T_{sat}} \tag{13}$$

where $\widetilde{M}$ and $\widetilde{R}$ are respectively the molecular weight and the universal gas constant. The accommodation coefficient $\hat{a}$ is defined as the ratio between the actual evaporation rate and the theoretical maximum phase change rate (Faghri 1995). Its value depends on the surface nature and state, but it is also affected by the composition and pressure of the gas mixture in the environment and other parameters. For these reasons, the values of $\hat{a}$ differ widely in literature and a precise evaluation of the accommodation coefficient is not trivial. Paul (1962) reported a collection of $\hat{a}$ values valid for many working fluids and Mills and Seban (1967) concluded that the accommodation coefficient should be smaller than unity when the fluid or the interface is contaminated.

Particle Level Model

Once the temperature and pressure fields are solved with the global wick model, it is necessary to include the effect of the meniscus shape along the evaporative boundary. The particle-level model, valid at the evaporative boundary, adds the boundary effect of the liquid-vapor interface on momentum and energy equations solved in the wick model.

Assumptions

The following assumptions are made:

1. Thermal steady-state, valid for operational cases where no transient phenomena, such as nucleation and boiling, take place.
2. Negligible convection in the liquid domain (only conduction), valid for low super-heats (Ranjan et al. 2009).
3. Negligible convection between the solid walls of the particle and the vapor. This interface can be considered adiabatic due to the very small effect of natural convection of vapor on the particle compared to the evaporative heat transfer (Ranjan et al. 2009).
4. Zero thickness of the liquid-vapor interface. The liquid and vapor thermal properties change across this interface.
5. Temperature at the liquid-vapor interface is the saturation temperature at the local static pressure.
6. Constant thermal properties.

The temperature T_b is equivalent to the average temperature at one particle diameter away from the evaporative boundary, as indicated in Fig. 3. It is assumed to be equal along the three sides of the domain for simplicity of the calculations. The effect of the temperature variation along the evaporative boundary is accounted when solving the wick model together with the particle model.

Along the evaporative boundary the 2D model captures the liquid-vapor interface between two circular bodies. Ranjan et al. (2009) analyze different geometrical layout configurations of the porous structure/liquid-vapor meniscus concluding that the thin-film area of the meniscus is the highest in the case of packed spheres on a surface, based on static equilibrium liquid meniscus shapes, but the area-averaged heat transfer coefficient at the interface was observed to be nearly the same for all the wick structures.

Mathematical Formulation

Figure 3 illustrates the computational domain of the heat transfer of a particle with radius r_{part} and a meniscus at an angular position α. The origin of the global coordinate system $(\hat{x}, \hat{y})$ is at the center of the left particle. Assuming no convection in the liquid phase, the mathematical formulation of the problem is the following:

$$\frac{\partial^2 T}{\partial \hat{x}^2} + \frac{\partial^2 T}{\partial \hat{y}^2} = 0 \tag{14}$$

and the boundary conditions are

$$\begin{cases} T(0,\hat{y}) = T_b & \text{for } \hat{x} = 0 \\ T(2r_{part},\hat{y}) = T_b & \text{for } \hat{x} = 2r_{part} \\ T(\hat{x},-r_{part}) = T_b & \text{for } \hat{y} = -r_{part} \\ -k_l \nabla T = h_{ev}(T - T_{sat}) & \text{at } \partial\Omega_{ev} \\ \nabla T = 0 & \text{at } \partial\Omega_{ad} \end{cases} \tag{15}$$

where r_{part} is the particle radius, T_b is the known temperature at the base of the particle and at the liquid inlet, T_{sat} is the saturation temperature and h_{ev} is the evaporative heat transfer coefficient, $\partial\Omega_{ev}$ and $\partial\Omega_{ad}$ are respectively the evaporative and adiabatic boundaries, as indicated in Fig. 3.

The relationship between α and meniscus radius is calculated as follows:

$$\frac{r_m}{r_{part}} = \frac{(1-\cos\alpha)}{\cos\alpha} \tag{16}$$

where r_m is the mean radius of the meniscus in the capillary pressure equation

$$P_c = P_{nw} - P_w = \frac{2\sigma}{r_m} \tag{17}$$

where P_{nw} and P_w are the non-wetting and wetting phases of two immiscible fluids.

Figure 4 illustrates the temperature mapping of a particle of radius $r_{part} = 50$ μm, meniscus angular position $\alpha = 60°$, temperature $T_b = 26.2$ °C, liquid thermal conductivity $k_l = 0.48$ Wm^{-1}K^{-1} and solid thermal conductivity $k_s = 80$ Wm^{-1}K^{-1}. The main temperature gradient is in the region below the evaporative boundary on the liquid side because of the high thermal conductivity of the solid particle. Figure 5 (top) shows the evaporative heat flux along the evaporative boundary $\partial\Omega_{ev}$ for a given T_b. The angular position α of the meniscus along the particle does not affect the maximum heat fluxes and temperature values, instead it influences the overall evaporative heat load due to the extension of the evaporative domain. As indicated in Fig. 5 (bottom), higher α angles lead to higher evaporative heat loads, however the actual limit depends on capillary pressure considerations. For instance, even if $\alpha = 90°$ would allow the highest evaporative heat load, the capillary pressure equal to zero (no curvature) would not create a condition of liquid flow from the bottom inlet to the liquid-vapor interface as indicated by Eq. 17.

During nominal conditions, the liquid mass flow rate $\dot{m}_l$, calculated through the Darcy's law and the capillary pressure, has to be equal to the vapor mass flow rate $\dot{m}_v$ produced at the liquid-vapor interface calculated by the particle model. This relationship can only be satisfied by a univocal meniscus radius or α angle at a given position along the evaporative boundary. Figure 6 summarizes the relationship between the base particle temperature T_b and the angular position α for different locations along the evaporative boundary of the wick domain. The base temperature T_b able to sustain a ratio $\frac{\dot{m}_l}{\dot{m}_v} = 1$ decreases with α up to the saturation temperature $T_{sat} = 26$ °C at $\alpha = 90°$, while it increases exponentially for α lower than 30° reaching 76 °C at $\alpha = 10°$. This means that dry-out is likely to occur in the wick at the boundary where the heat input is applied than at the evaporative boundary.

Algorithm

The heat and mass transfer calculations for the porous structure are carried out through a 2D Finite Difference scheme built in MATLAB (Quickersim-CFD-Toolbox 2024) and counts 10^5 elements throughout the domain with a spatial resolution of 0.01 mm per cell. The algorithm takes as input parameters: pressure and temperature on the liquid side, pressure in the vapor groove, imposed heat flux at the top boundary of the pillar and material properties from the REFPROP Thermal Fluid Properties Database (Lemmon et al. 2018).

After an initial guess on the temperature field, the pressure field within the porous domain Ω is solved with the Dirichlet condition at the convective boundary and the evaporative boundary condition (Eq. 11 at the liquid-vapor interface). Knowing the pressure field, velocity is calculated

Fig. 4 Temperature mapping within the particle model

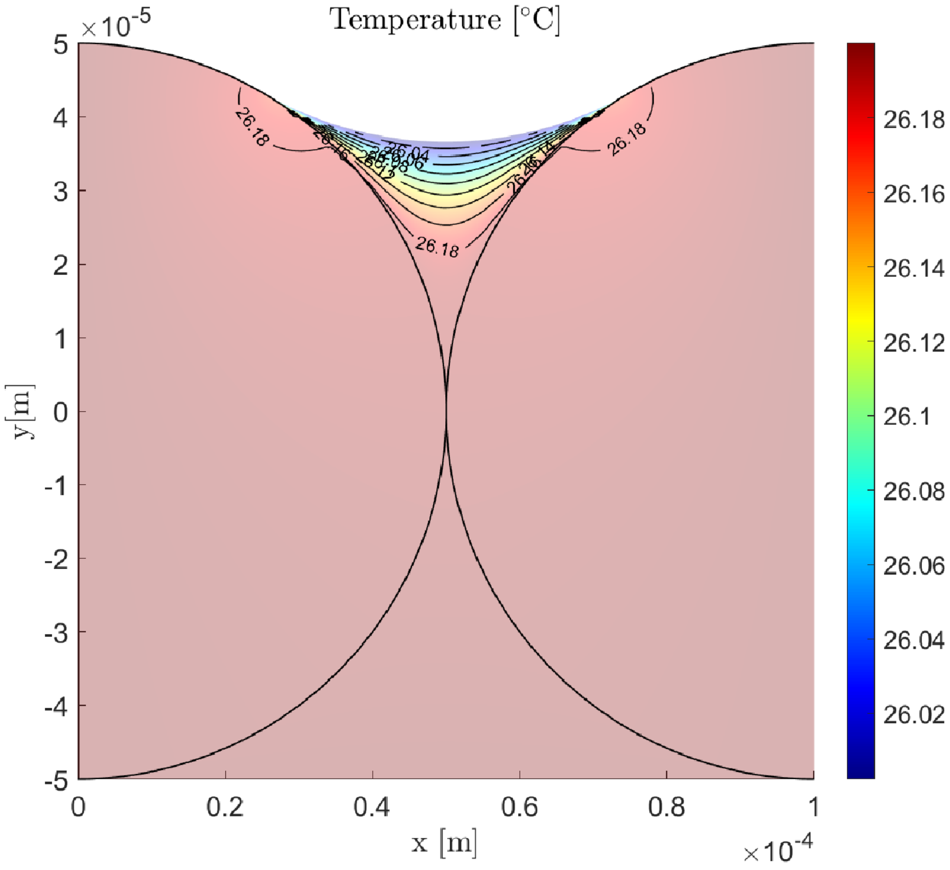

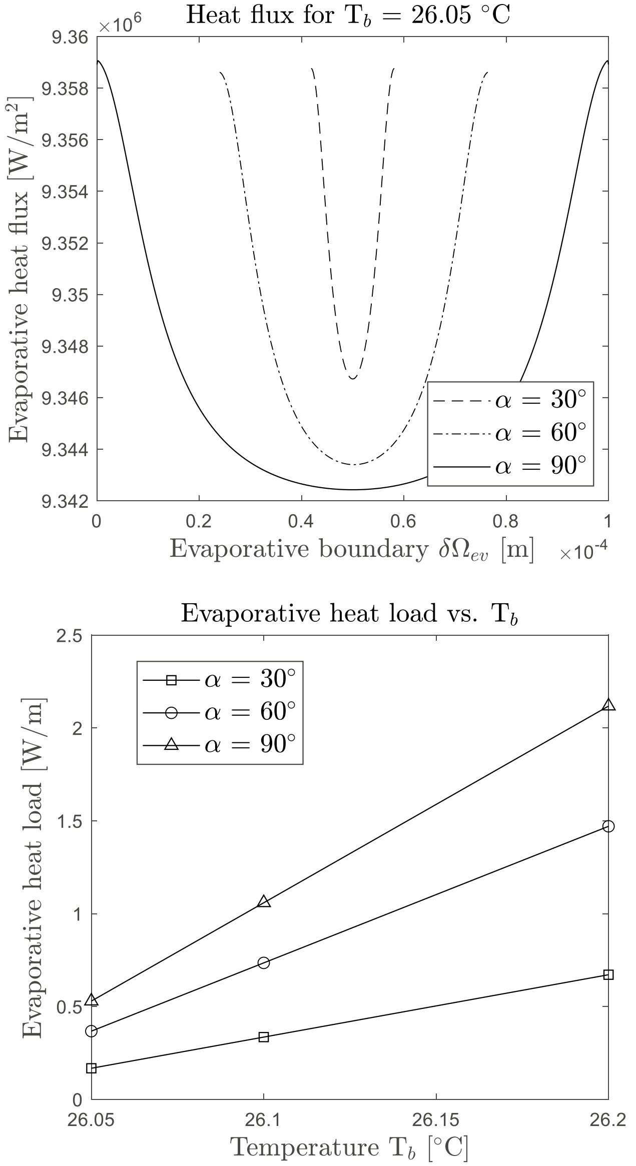

Fig. 5 Evaporative heat flux along the interface $\delta\Omega_{ev}$ for a given T_b (top). Evaporative heat load per particle as function of T_b (bottom)

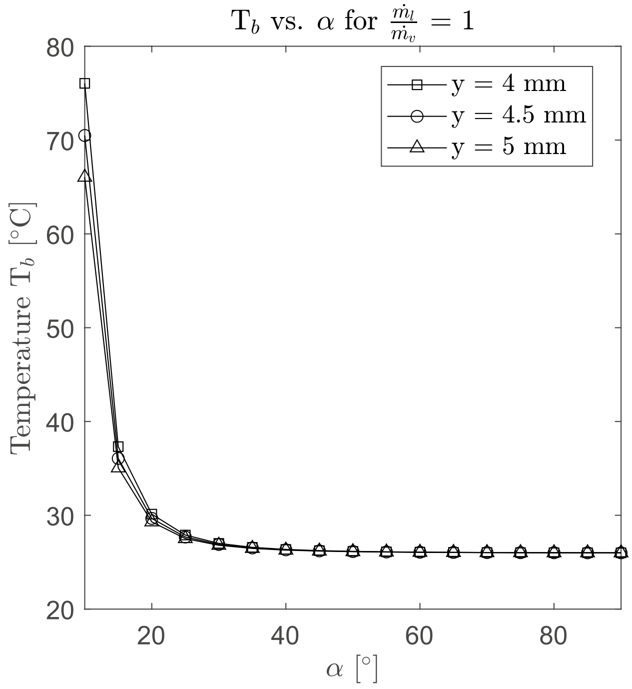

Fig. 6 T_b as function of α at different locations along the evaporative heat boundary of the wick model

using the Darcy's law. The advection-diffusion equation for the temperature field is solved assuming convective heat transfer at the liquid chamber, imposed heat flux at the top of the wick pillar and evaporative heat flux along the wick-vapor interface. The convergence criteria are achieved when the maximum relative change of temperature is less than 10^{-4} °C and the energy balance reaches the imposed tolerance of 10^{-8}. The temperature profile located at one particle diameter under the evaporative boundary is extracted once the model has converged. This temperature profile becomes the input to relationship between the evaporative heat load and the base temperature T_b calculated through the particle model with the condition that the liquid mass flow rate $\dot{m}_l$ has to be equal to the vapor mass flow rate $\dot{m}_v$. The new evaporative heat load along the evaporative boundary is calculated and becomes the new boundary condition to the wick model for the energy field. The process is re-iterated till convergence.

The heat and mass transfer within the porous structure and, in particular, the evaporative heat loads are calculated using the following procedure:

(i) Initialize the input parameters such as boundary conditions, fluid and wick properties, geometrical domain.
(ii) Solve the momentum equation with the applied boundary conditions.
(iii) Calculate the velocity field using Darcy's law.
(iv) Solve the energy equation with the appropriate boundary conditions.
(v) Re-iterate till convergence criteria indicated above are satisfied.
(vi) Extract the temperature profile parallel to the evaporative boundary at a distance equivalent to one particle diameter.
(vii) Split the temperature profile extracted in (vi) into $N = 15$ elements equal to the ratio between the length of evaporative boundary and the particle diameter.
(viii) Based on the relationships between T_b and α calculated through the particle-level model with the condition $\frac{\dot{m}_l}{\dot{m}_v}$

= 1, calculate the new evaporative heat load along the evaporative boundary.

(ix) Re-iterate the calculation of the momentum and temperature fields in the wick model using the new evaporative heat load profile.

(x) Re-iterate till convergence criteria indicated above are satisfied.

Experimental Setup

The experimental setup was built in order to investigate the heat transfer behaviour of the porous structure thermally driven by phase change phenomena and capillary forces. The main objectives were:

- Experimental quantification of the evaporative heat load generated at the liquid-vapor interface.
- Validation of the numerical model under steady-state conditions.
- Investigation of the dry-out condition (transient) on the heat transfer and performance of the evaporator.

Figure 7 presents the fluid loop of the experimental setup of a titanium AM evaporator. The evaporator is connected to a liquid reservoir to supply sub-cooled liquid to the porous structure. The hydrostatic pressure drop is regulated by controlling the elevation Δh between the top surface of the wick and liquid level in the reservoir. A temperature controller regulates the temperature in the liquid chamber of the test cell through a heating tape placed along the tube connecting the reservoir and the evaporator. The top surface of the wick is heated with a tape heater. The AM sample is enclosed by transparent acrylic walls with a 20 mm thickness. The vapor exiting the test cell passes through a condenser and is collected in a flask. The mass of condensate is measured over time. The test cell is surrounded by a 10 mm air gap followed by a 10 mm thermal insulation in order to reduce heat losses to the ambient. Twenty calibrated t-type thermocouples are located in the porous and solid titanium. Several thermocouples are installed on the external walls of the test cell, in the liquid chamber, at the outlet of the vapor chamber and in the condenser. The system is composed of a power supply and a data acquisition system (DAQ).

Test Cell

The test sample was fabricated at JPL using the Powder Bed Fusion Additive Manufacturing (AM) technique (Gotoh et al. 2022). It is made of a solid top layer of 10 mm thick and a porous structure of 50 mm height, contained within an acrylic case, as illustrated in Figs. 7 and 8. Table 3 summarizes its main porous properties. The titanium sample was printed horizontally on a steel substrate and then removed through the wire electron discharge machining (wire EDM). This manufacturing process allows to cut a desired shape within ± 1 µm using discharges across a fine wire minimizing the alteration of the back surface of the porous sample. After the machining, the sample was cleaned in an ultrasonic resonator in an acetone bath to remove any residual dust.

The AM sample is surrounded by one mm silicone pad that prevents any parasitic liquid flow from the bottom liquid chamber to the top. An air gap of 10 mm is present between

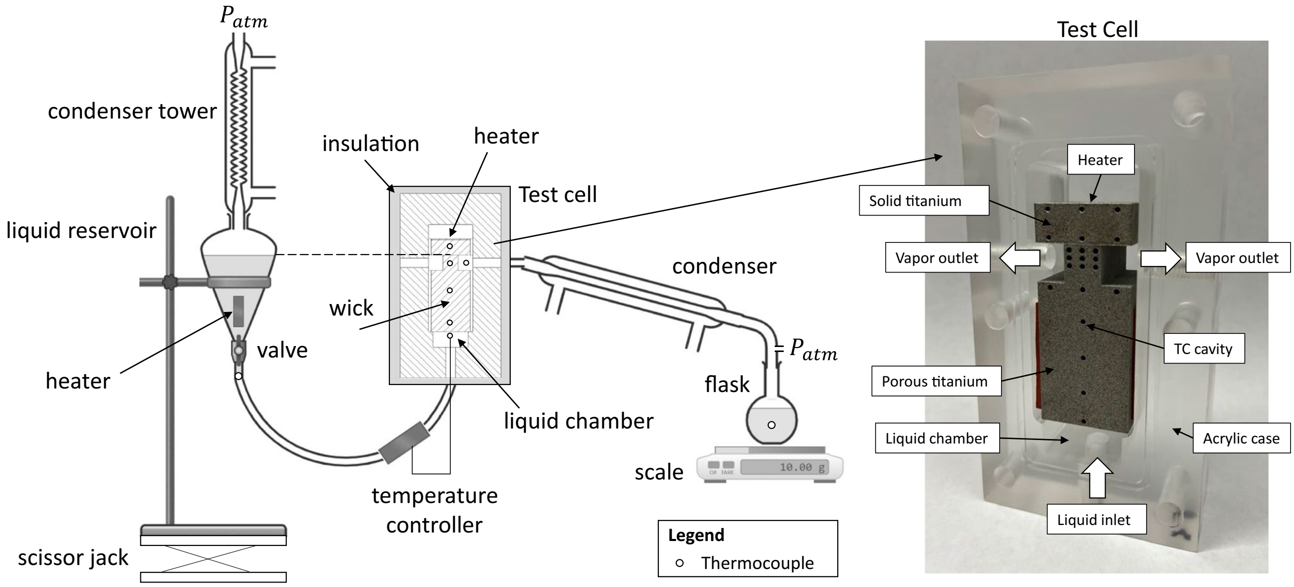

Fig. 7 Experimental layout of the titanium AM evaporator (left). Photo of the test cell (right)

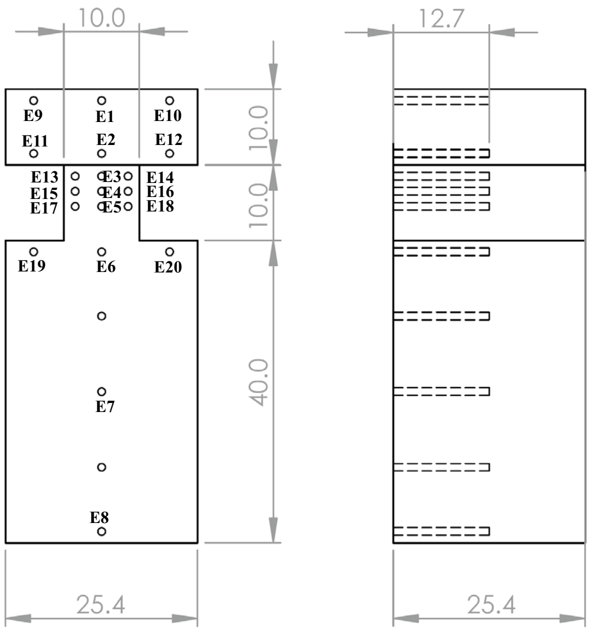

Fig. 8 Drawing of the AM titanium sample (dimensions in mm). Front (left) and side (right) views with location and ID of the thermocouples

the acrylic walls of the case and a 10 mm K-flex thermal insulation, allowing to reduce heat losses to the ambient.

During nominal operation, heat is applied at the upper surface of the test cell and transferred to the wick medium filled with the working fluid, Galden PFPE-70. The fluid properties are summarized in Table 4. The heater can provide a heat load up to 10 W. The evaporator temperature cannot exceed 100 °C in order to reduce any chances of delamination of the foil heater. The liquid chamber at the bottom of the wick is at a known pressure and subcooled liquid is continuously provided by the liquid reservoir. In order to sustain continuous capillary flow, the maximum capillary pumping pressure $2\,\sigma/r_e$, where r_e is the effective pore radius, must meet or exceed the sum of all pressure drops.

Measurement Techniques

T-type thermocouples were carefully calibrated with the complete measurement chain over the temperature range investigated prior to the measurement against a PT100 temperature probe as reference temperature. From the recorded temperatures a calibration polynomial was built. All the thermocouples were found to be within ± 0.1 °C from the reference temperature. The thermocouples were installed inside 12.5 mm cavities in the AM sample. A mixture of epoxy and silver paste was inserted inside the cavities with two different syringes, then the hot junction of the thermocouples was inserted and let it harden for 48 h. The cold junction of the thermocouples was placed into an ice bath to minimize the effects of the ambient temperature on the DAQ.

Table 3 Porous properties of the selected titanium sample

Alloy	r_p [µm]	ϵ [%]	K [m^2]
Titanium	15.7	18.5	5.6 x 10^{-13}

Table 4 Thermal properties of Galden PFPE HT-70 at 1 atm (Lemmon et al. 2018)

Property	Unit	Value
Boiling point	°C	70
Density	kg m^{-3}	1680
Kinematic viscosity	m^2 s^{-1}	5 x 10^{-7}
Specific heat	J kg^{-1} K^{-1}	963
Heat of vaporization	kJ kg^{-1}	71.2
Surface tension	N m^{-1}	0.014
Thermal conductivity	W m^{-1} K^{-1}	0.065
Average molecular weight	amu	410

The condensed liquid was collected in a flask and its mass measured at the end of each run by a high precision scale with ±0.01 g resolution. The temperature of the condensate was also recorded over time.

To remove the air from the wick structure, prior to each test run, the liquid level in the reservoir was adjusted slightly to the top of the porous structure and heat load was applied to keep at saturation conditions the top surface of the porous pillar. Then, the liquid level at the reservoir was adjusted to the required elevation Δh between the top surface of the wick and liquid level in the reservoir.

An uncertainty analysis was performed following the uncertainty estimation method (Kline 1963). The heat input can be expressed as function of the applied voltage V and heater resistance R:

$$Q_{in} = \frac{V^2}{R} \tag{18}$$

and the relative uncertainty w_Q of Q_{in} is

$$w_Q = \sqrt{\left(\frac{dQ}{dV} w_V\right)^2 + \left(\frac{dQ}{dR} w_R\right)^2} \tag{19}$$

where w_V and w_R are respectively the relative uncertainties of the voltage and heater resistance.

The evaporative heat load is measured as

$$Q_{ev} = \dot{m}_l h_{fg} \tag{20}$$

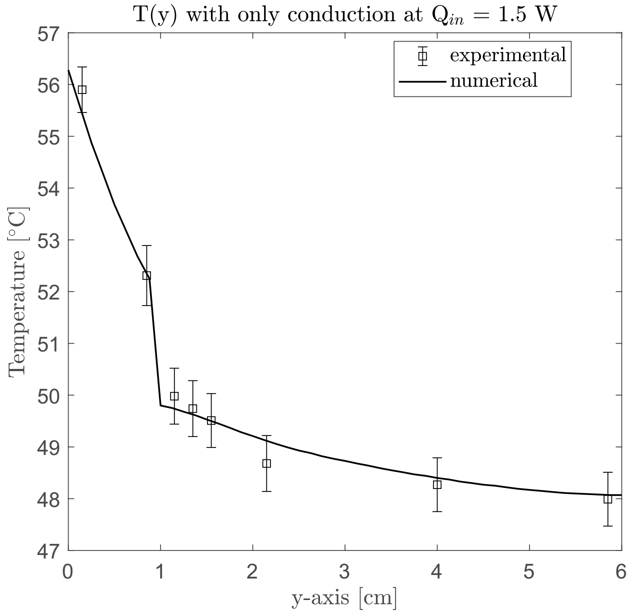

Fig. 9 Temperature along the y-axis with an inlet power of 1.5 W (pure conduction)

where $\dot{m}_l$ is the liquid collected at the flask after the condenser over the time of the test run. At least 100 g are collected per run and it is conservatively assumed that around 5 g are trapped along the path from the vapor chamber to the flask. The Root Sum of Squares (RSS) analysis indicates that the resulting uncertainty in the heat input measurement is 1.5% of the total applied heat load and the uncertainty of evaporative heat load is 5% of the input heat load.

Experimental Validation

Preliminary tests, based on pure conduction, were conducted in order to assess the actual thermal properties of the AM sample, such as thermal conductivity and contact resistance between the solid and the porous structure. Consequently, the numerical model was adjusted to reflect the experimental results with an effective thermal conductivity of the porous domain equal to 5.5 W m^{-1} K^{-1} and a corrected thermal conductance at the solid-to-porous interface of 0.1 W cm^{-2} K^{-1}. Figure 9 illustrates the temperature profile along the y-axis (symmetry axis) and the effect of the thermal contact resistance between the solid and porous parts of the titanium sample (located at $y = 1$ cm).

In case of pure conduction (no liquid in the porous structure), the energy balance indicates that, out of 1 W that goes into the porous structure, 0.4 W are the heat losses towards the case and the thermocouples. Tests were repeated 5 times per each power input. The standard deviation observed in the conduction tests is 0.15–0.4 K (value varying depending on heat input). Each test was carried out for a minimum duration of 5 h to reach steady-state. Then the steady-state data was collected for 2 h.

Results and Discussion

Numerical Evaluation of the Heat Transfer within the 2PMPL Evaporator

The baseline configuration of the 2PMPL evaporator (Furst et al. 2018) has a 4 mm thick porous base and 1 mm high porous pillar. The aluminum wick is fully saturated with liquid ammonia. Pressure in the liquid chamber and in the vapor groove is at 10.345 bar, while temperature at the liquid inlet is 24 °C and the saturation temperature T_{sat} is equal to 26 °C. Table 5 summarizes its main inputs given to the numerical model in terms of boundary conditions, wick properties and geometrical parameters.

The numerical simulations indicate that the maximum temperature occurs at the upper-left corner, as shown in Fig. 10. Fluid flow is nearly one-dimensional throughout the wick, except in proximity of the boundary where the heat load is applied, and the x-component of velocity becomes important.

Along the evaporative heat boundary the angular position α of the liquid-vapor interface increases till reaching 90° where no evaporation takes place, as presented in Fig. 11. Higher is the imposed heat flux, lower is the corresponding α at a given location along the evaporative boundary.

Figure 12 shows the temperature profile along $x = 0$ for different heat fluxes applied at the top edge of the wick pillar. It is noted that the temperature gradient is significant in the region of the wick pillar. For imposed heat fluxes of 4 and 6 W cm^{-2}, the maximum temperatures in the domain are respectively 26.2 and 26.4 °C. Figure 13 illustrates that the temperature along the evaporative boundary is slightly above the saturation temperature of 26 °C as expressed by Eq. 12. The majority of heat transfer is occurring in the first top half of the pillar boundary (within 0.5 mm).

Experimental tests on the evaporator show that the measured dry-out occurs at about 5 W cm^{-2}. This suggests that a pore radius distribution of about 3.8 µm is located in the porous pillar. When evaporation takes place, the evaporative heat transfer depends on liquid supply to and vapor escape from the liquid-vapor interface. The nucleation limit mainly depends on the maximum temperature at the top left-hand corner of the wick structure and the pressure drop over the structure due to the capillary limits. To avoid bubble formation, the difference between the maximum temperature in the wick and the saturation temperature must be lower than the minimum superheat for the onset of bubble formation indicated by the Clausius-Clapeyron equation.

Table 5 Boundary conditions, wick properties and geometrical inputs to the numerical model

Parameter	Units	Value
Liquid temperature	°C	24
Liquid pressure	bar	10.34
Conv. heat transfer coeff.	W m^{-}2 K^{-}1	1900
Vapor pressure	bar	10.34
Sat. temperature	°C	26
Evap. heat transfer coeff.	W m^{-}2 K^{-}1	3.98 x 10^6
Eff. thermal cond.	W m^{-}1 K^{-}1	56
Porosity	%	22.3
Permeability	m^{-}2	3.2 x 10^{-13}
Eff. pore radius	μm	3.8
L_x	mm	1
L_y	mm	4
L_{xp}	mm	0.5
L_{yp}	mm	1

In this system configuration (assuming an uniform 3.8 μm effective pore radius), nucleation in the wick begins when the superheat $T - T_{sat}$ in the wick exceeds 0.35 °C,

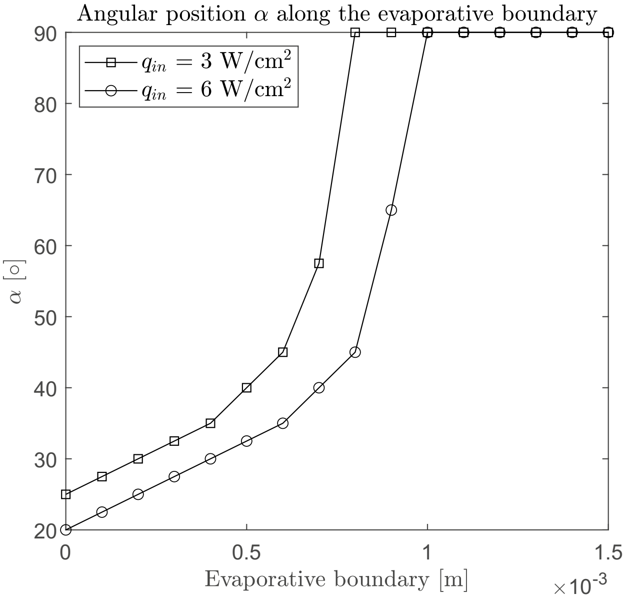

Fig. 11 Angular position α of the meniscus along the evaporative boundary for different q_{in}

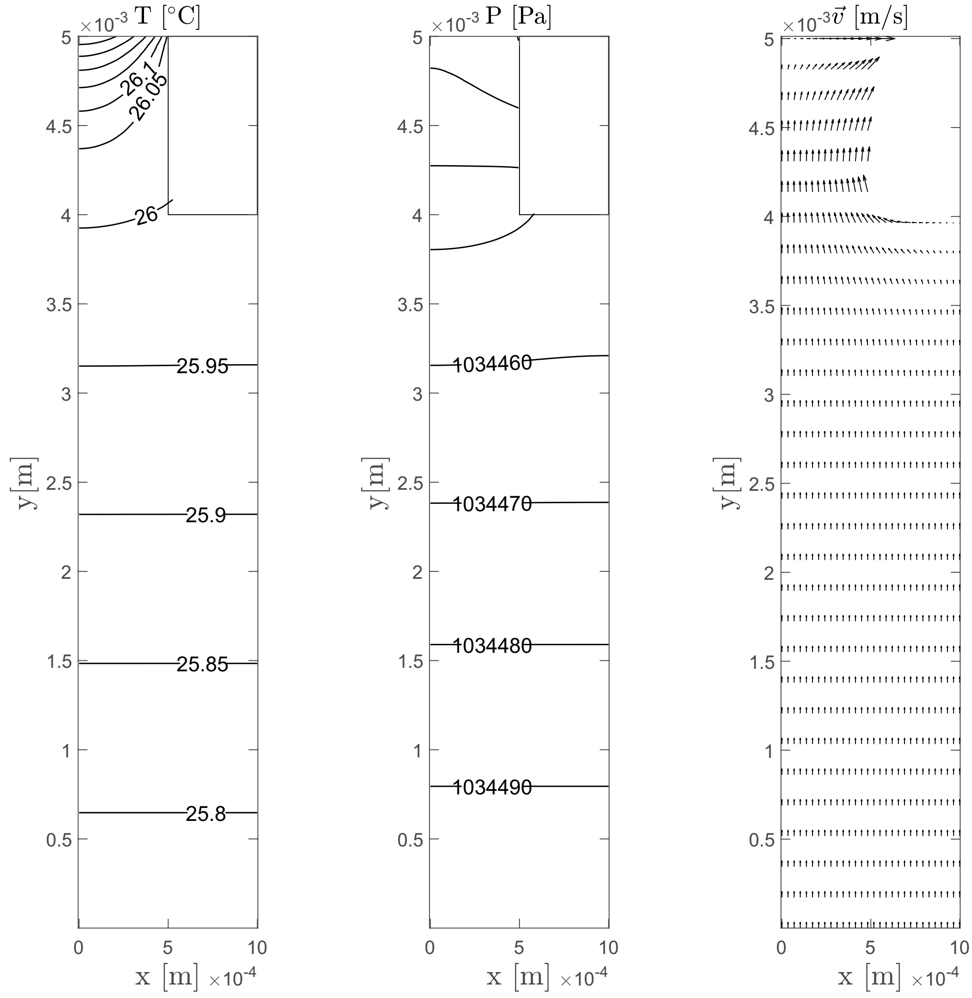

Fig. 10 Temperature, pressure and velocity mapping along the porous domain with input heat flux q_{in} = 5 W cm^{-2}

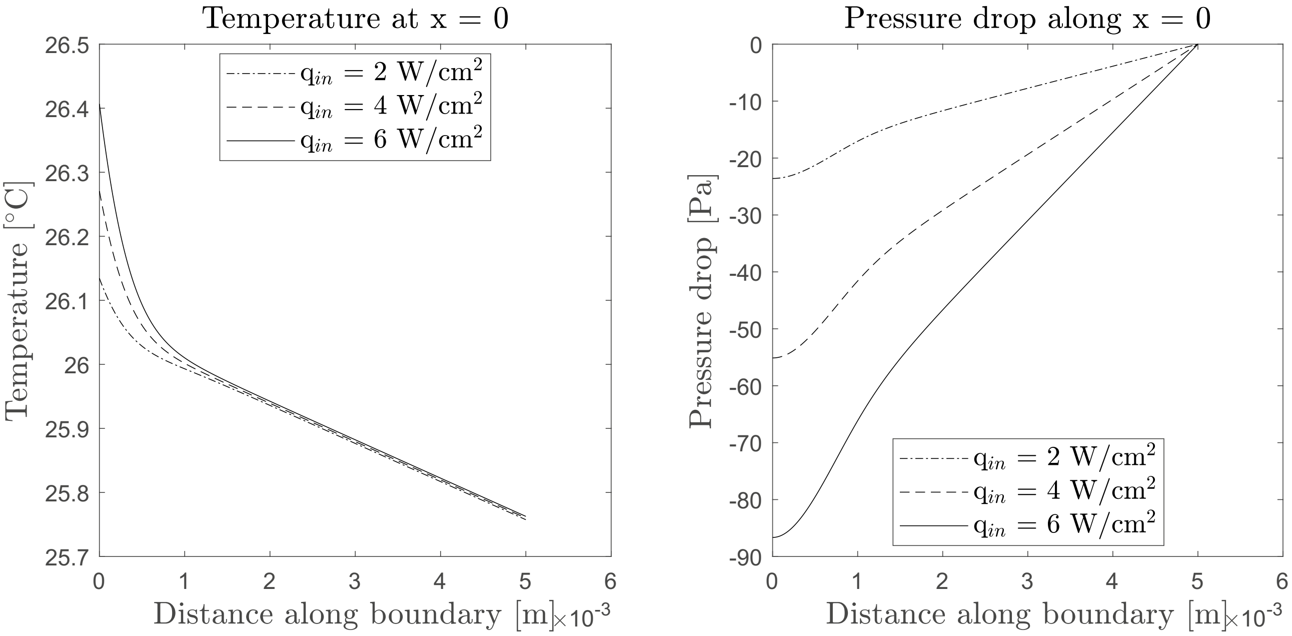

Fig. 12 Temperature and pressure profiles along the y-axis for different q_{in}

equivalent to an input heat flux of 5 W cm^{-2}. The superheat required for nucleation is inversely proportional to the pore radius. A porous structure with a reduced pore size would allow an increase of the maximum heat flux (up to 16.5 W cm^{-2} for one µm effective pore radius). On the other hand, a compromise is generally required between pore size distribution and permeability since smaller is the pore size lower is the permeability of the porous structure.

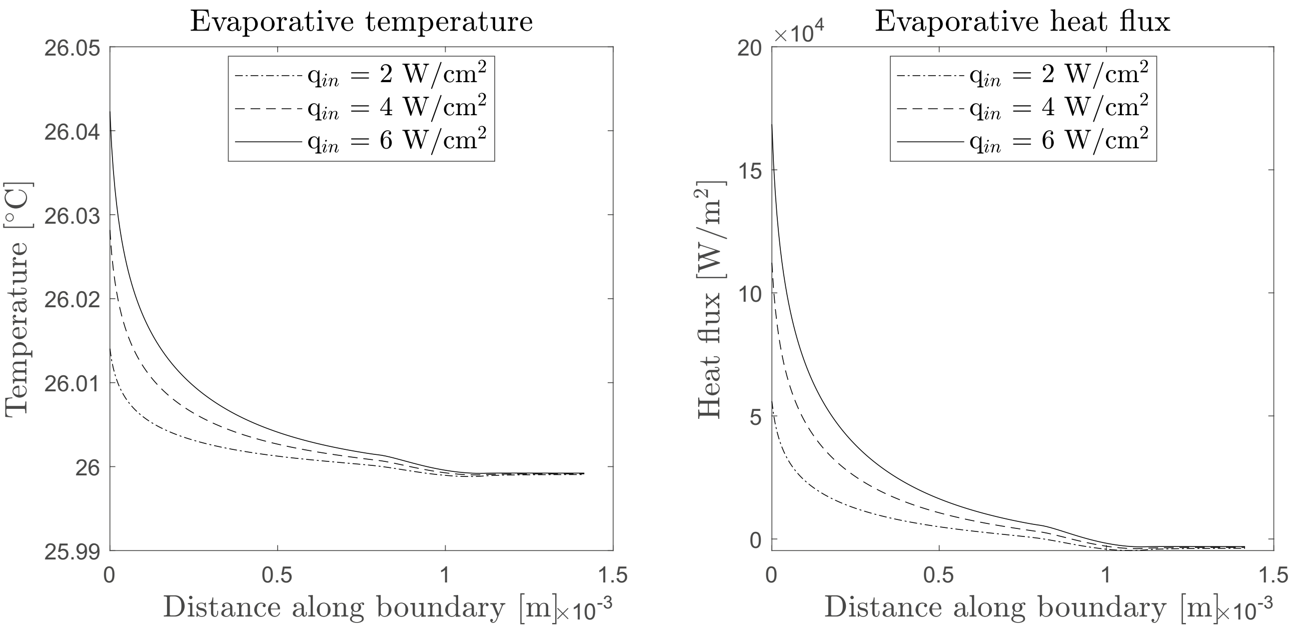

Fig. 13 Temperature and heat flux profiles along $\partial\Omega_{ev}$ for different q_{in}

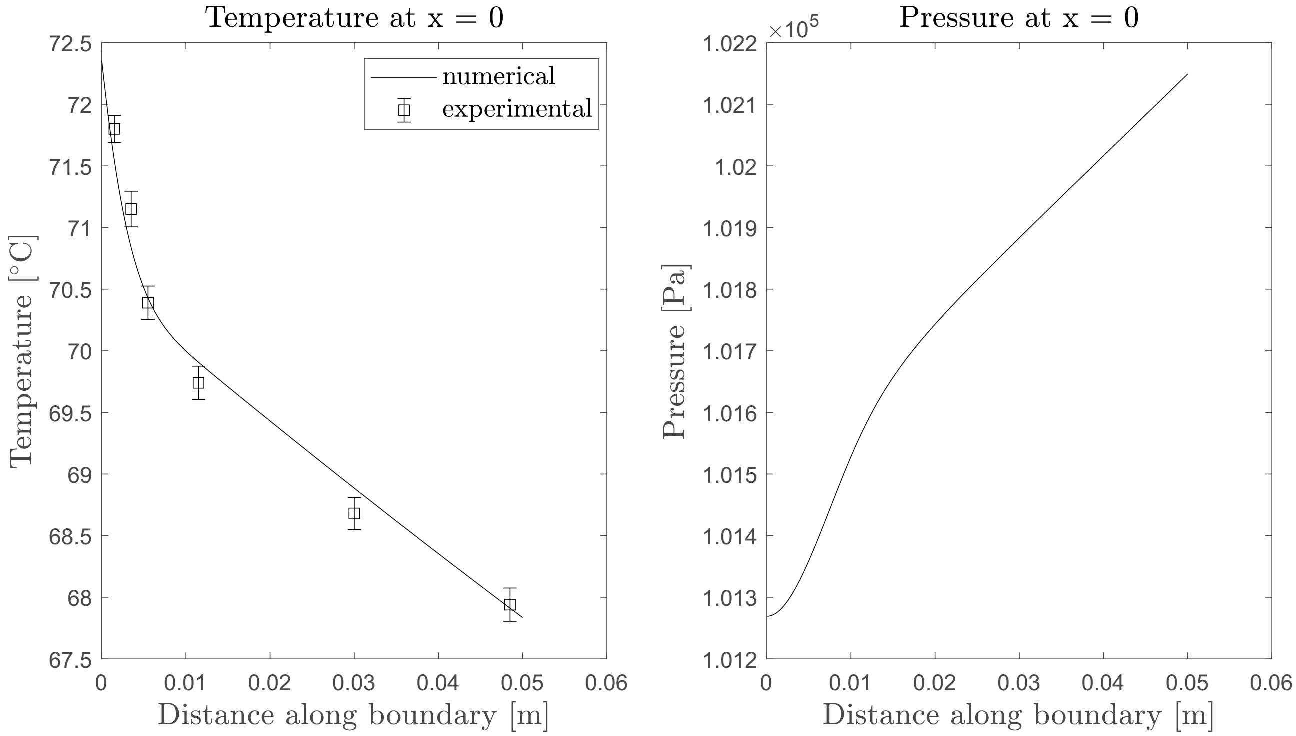

Fig. 14 Temperature and pressure profiles along the y-axis for $Q_{in} = 4$ W

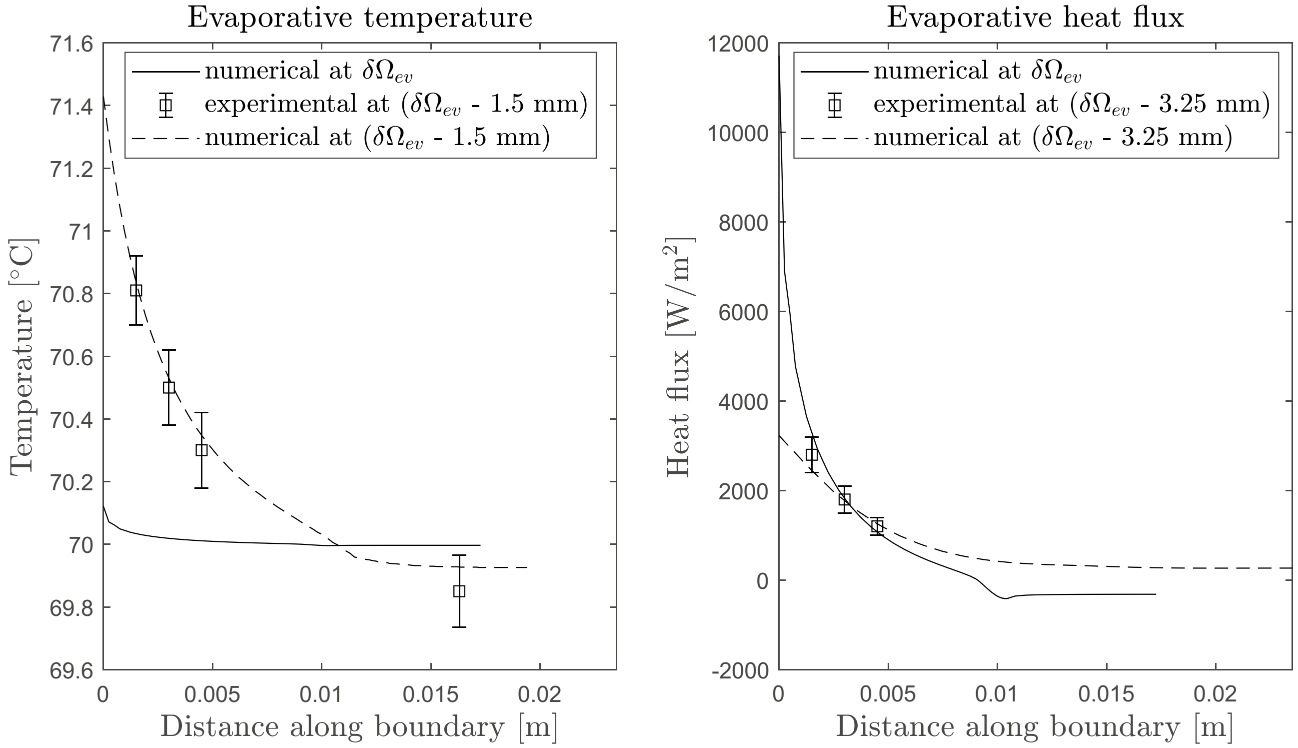

Fig. 15 Temperature and heat flux profiles along $\partial\Omega_{ev}$ for $Q_{in} = 4$ W

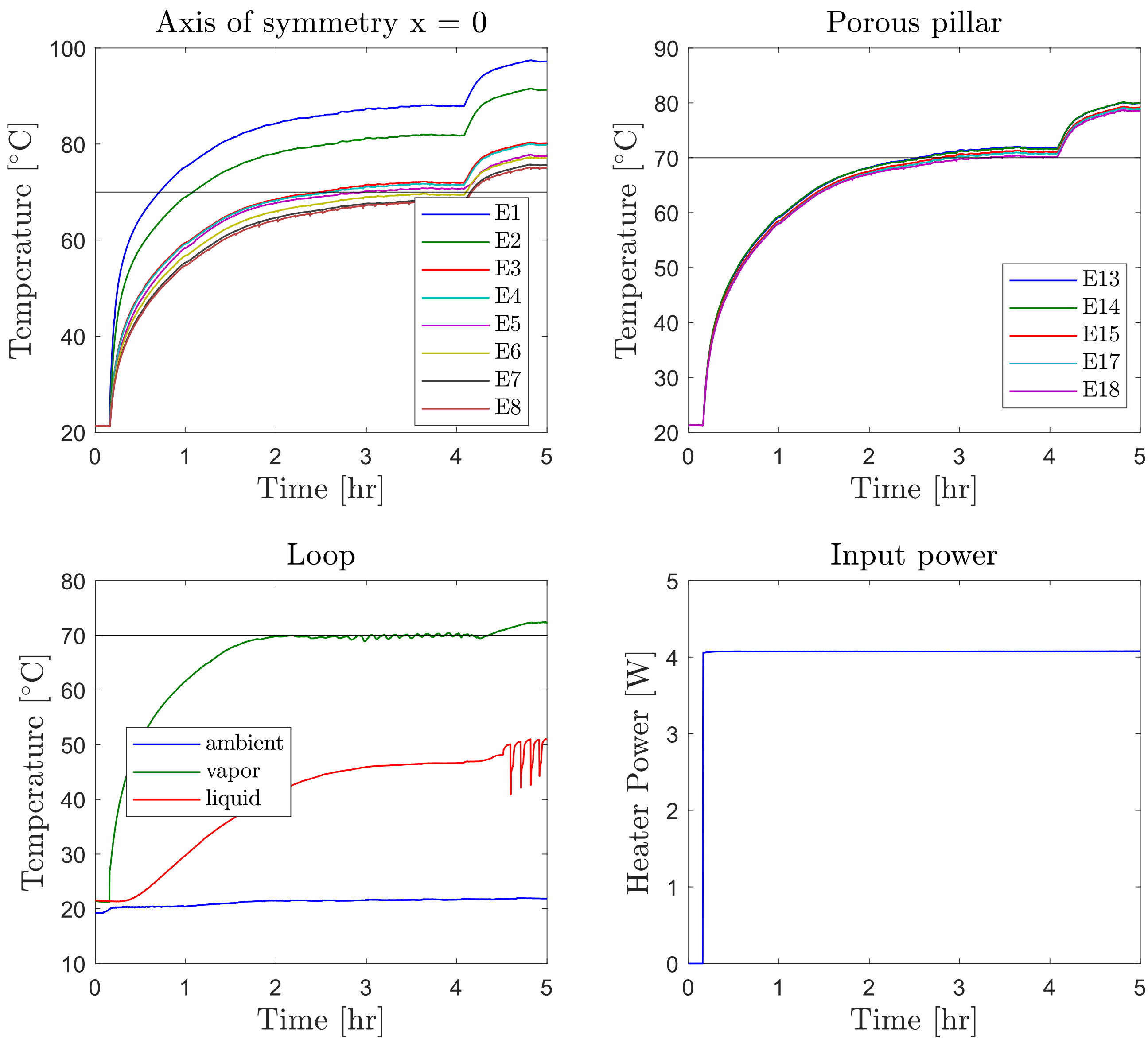

Fig. 16 Thermal transient with inlet power of 4 W and Δh = [0, 1] cm

Comparison of Numerical and Experimental Results at Thermal Steady-State

The numerical model used for the experimental campaign includes the presence of contact resistance at the interface solid-to-porous, the corrected thermal conductivities, and the effect of gravity. When the elevation distance Δh equals zero, the inlet pressure is 1.008 atm, while the outlet pressure is at 1 atm. The evaporative heat transfer coefficient is calculated in agreement with Eq. 13 with constant thermal properties at 1 atm and its value corresponds to 9.6 x 10^4 W cm^{-2} K^{-1}. The accommodation coefficient (assumed equal to 1) affects the temperature gradient along the evaporative boundary and the total pressure drop along the wick. Effects are negligible on the temperature profiles along the axis of symmetry x = 0 (Valdarno 2022).

The standard deviation observed in the evaporation test (with liquid flow through the porous media due to capillarity) is 0.15 - 0.3 K (value varying depending on heat input). Each test was carried out for a minimum duration of 5 h to reach steady-state. Then the steady-state data was collected for 2 h. Tests were repeated 5 times for the 4 W heat input case and 3 times for the other cases since no significant variation (in the mean value and standard deviation) between tests were observed.

Figure 14 illustrates the temperature and pressure profiles along the axis of symmetry $x = 0$. It is noted that only a 4 °C temperature gradient (4.5 °C) is present between the top and bottom boundary of the wick structure. As expected, the liquid flow along the domain is mostly one dimensional in the base of the wick and becomes 2D in proximity of the liquid-vapor interface. Figure 15 (left) presents the temperature profiles along the evaporative boundary (only num.) and at 1.5 mm underneath the surface where the thermocouples are located (both num. and exp). The temperature gradient at 1.5 mm below the evaporative surface is 1.5 °C). The numerical model indicates a good agreement with the measured temperature (standard deviation is 0.15 °C). Figure 15 (right) shows the comparison between the numerical and experimental heat fluxes (calculated based on temperatures recorded by the TCs located at the center of symmetry of the pillar and at 1.5 mm below the evaporative surface). The numerical and experimental temperature profiles present a good agreement. It is understood that under the current experimental arrangement only the numerical model can provide the accurate temperature profile and heat flux along the evaporative boundary.

The energy balance indicates that out of 4 W applied at the foil heater, 3 W go to the top boundary of the porous media (q = 0.5 W cm^{-2}), the total heat losses are 0.8 W (26% of total heat input: 0.65 W towards the case and 0.15 W towards the liquid). The experimental evaporative heat load was calculated as the ratio between the measurement of the condensed liquid over a certain time and the latent heat. The numerical model confirms that the heat load to evaporation is 2.2 ± 0.1 W.

Experimental Thermal Transient: Dry-Out Events

The experimental effort allowed the characterization of the transient conditions, such as dry-out. Figure 16 shows a test run with an inlet heat load of 4 W at an elevation of Δh = 0 cm. Thermocouples E1-E2 and E3-to-E8 are located along the center of symmetry respectively in the solid and porous sections of the AM sample, as shown in Fig. 8. In the first part of the test, the evaporator reaches a thermal steady-state condition after 4 h, while in the second part the elevation Δh is suddenly increased up to 1 cm (located at the base of the wick pillar). As a consequence, all temperatures increase and it is noted that thermocouple E8 (located at 1.5 mm inside the bottom surface of the wick) reaches a temperature of 76 °C above the saturation temperature of 70 °C. The temperature recorded in the middle of liquid chamber oscillates and the temperature in the vapor chamber increases above saturation. The experimental results suggest that not only dry-out takes place at the top of wick pillar due to temperature values way above the nucleation limit, but also bubbles at the bottom interface of the wick are formed and merged in a single slug, forcing the oscillation of temperature recorded by the thermocouple located at the center of the liquid chamber. During this phase no liquid condensation is observed at the collecting flask.

Such increase of the temperatures of the solid and wick parts can be explained due to the penetration of the vapor within the porous structure caused by the adverse hydrostatic pressure. In particular, an increase of the hydrostatic pressure drop reduces the supply of the liquid at the liquid-vapor interface. The vapor expands in the wick invading more pores, the temperature of the case increases and the heat transfer performance is degraded. An increase in Δh leads to a decrease of the liquid mass flow rate that feeds the top boundary of the wick and causes an overheating of the casing. Moreover, it is interesting to notice that failure does not come only from the dry-out at the top region, but also from the fact that the bottom base of the wick reaches saturation conditions with consequent nucleation and bubble expansion inhibiting the liquid supply to the porous structure.

Conclusions

The numerical tool for the heat transfer within the wick facilitated the understanding of the physical aspects of the heat and mass transfer within the porous structure of an evaporator. The numerical model is based on continuity, momentum and energy equations together with a particle model valid at the liquid-vapor interface along the wick-to-vapor groove boundary. The experimental results validate the numerical calculations and contribute to the investigation of the transient behaviors of a capillary driven titanium evaporator. A good agreement is obtained between the experimental and numerical results. The main conclusions of this effort can be summarized as follows:

1. During nominal conditions, evaporation occurs along the wick-to-vapor groove interface with variable intensity, increasing in proximity of the heat source. Heat transfer is a result of the combination of evaporation, heat conduction within the porous media and convection to the cooling working liquid.
2. Dry-out at the wick-to-vapor groove boundary due to recession of the meniscus within the solid particles takes place at high superheat values. This implies that dry-out is likely to occur in the wick at the boundary where the heat input is applied rather than at the evaporative boundary.
3. The operational conditions of the porous structure subject to a heat input are limited by three main conditions: (1) capillary limit, caused by the insufficient capillary pressure at the liquid-vapor interface that is able to bring enough liquid flow to the evaporating surface; (2) nucleation limit, due to vapor bubble generation within the wick originated by a high input heat flux; (3) bub-

ble nucleation and vapor expansion at the liquid inlet surface causing a dry-out of the entire wick with little or no condensation.

4. The adverse hydrostatic pressure acting on the porous structure inhibits the liquid mass flow rate from the liquid chamber to the evaporating boundary. This causes bubble nucleation and vapor expansion towards adjacent pores with resulting temperature increase of the casing and the wick and degradation of the overall heat transfer performances.

Nomenclature

Greek Symbols α: Angular position of the meniscus along the particle (°); ϵ: Porosity (%); μ: Dynamic viscosity (Pa s); ρ: Density (kg m^{-3}); σ: Surface tension (N m^{-1})

Roman Symbols $\dot{m}$: Mass flow rate (g s^{-1}); $\hat{a}$: Accommodation coefficient (−); $\widetilde{M}$: Molar mass (kg mol^{-1}); $\widetilde{R}$: Universal gas constant (J K^{-1} mol^{-1}); A: Surface area (m^2); c_p: Specific heat (J K^{-1}); h: Heat transfer coefficient ((W m^{-2} K^{-1}); h_{fg}: Latent heat of evaporation (J kg^{-1}); K: Permeability (m^2); k: Thermal conductivity ((W m^{-1} K^{-1}); Nu: Nusselt number (−); P: Pressure (Pa); Pr: Prandtl number (−); Q: Heat load (W); q: Heat flux (W m^{-2}); r: Radius (m); Re: Reynolds number (−); T: Temperature (°C); u, v, w: Components of velocity along axis coordinates (m s^{-1}); x, y, z: Axis coordinates (m)

Subscripts cap: Capillary; e: Effective; ev: Evaporation; l: Liquid; p: Pore; $part$: Particle; s: Solid; sat: Saturation; v: Vapour

Acknowledgements This research was carried out at University of California, Los Angeles (UCLA) in collaboration with Jet Propulsion Laboratory (JPL) / California Institute of Technology, under a contract with the National Aeronautics and Space Administration. The authors are thankful to Thomas Beres and Ananthakrishnan Bhagyarajan for their assistance during the tests at UCLA and to Scott Roberts at JPL who coordinated the fabrication of the additively manufactured samples.

Author Contributions All four authors contributed to the effort. Dhir Sunada and Furst provided general guidance for research. The paper was mostly written by Valdarno

Funding All authors, except Vijay K. Dhir, were employed by Jet Propulsion Laboratory / California Institute of Technology under a contract with the National Aeronautics and Space Administration.

Availability of Data and Material Not applicable.

Declarations

Ethics Approval Not applicable.

Competing Interests The authors declare no competing interests.

References

Carman, P.C.: Fluid flow through a granular bed. Trans. Inst. Chem. Eng. London **15**, 150–156 (1937)

Faghri, A.: Heat pipe science and technology. Global Digital Press (1995)

Figus, C., Le Bray, Y., Bories, S., et al.: Heat and mass transfer with phase change in aporous structure partially heated: continuum model andpore network simulations. Int. J. Heat Mass Transf. **42**(14), 2557–2569 (1999)

Furst, B., Cappucci, S., Daimaru, T., Sunada, E., Roberts, S., O'Donnell, T.: An additively manufactured evaporator with integrated porous structures for two-phase thermal control. 48th International Conference on Environmental Systems (2018)

Gorring, R.L., Churchill, S.W.: Thermal conductivity of heterogeneous materials. Chem. Eng. Process. **57**(7), 53–59 (1961)

Gotoh, R., Furst, B., Roberts, S.N., et al.: Experimental and analytical investigations of AlSi10Mg, stainless steel, Inconel 625 and Ti-6Al-4V porous materials printed via powder bed fusion. Prog. Addit. Manuf. **7**(5), 943–955 (2022)

Kline, S.: Describing uncertainties in single-sample experiments. Mech Eng **75**, 3–8 (1963)

Lemmon, E.W., Bell, I.H., Huber, M.L., et al.: REFPROP documentation. Release **10**, 135 (2018)

Mills, A., Seban, R.: The condensation coefficient of water. International Journal of Heat and Mass Transfer **10**(12), 1815–1827 (1967)

Paul, B.: Compilation of evaporation coefficients. ARS J. **32**(9), 1321–1328 (1962)

QuickerSim: QuickerSim CFD toolbox. MATLAB Central File Exchange (2024). https://www.mathworks.com/matlabcentral/fileexchange/71604-quickersim-cfd-toolbox. Retrieved 3 Jun 2024

Ranjan, R., Murthy, J.Y., Garimella, S.V.: Numerical study of evaporation heat transfer from the liquid-vapor interface in wick microstructures, vol. 43826, pp. 1323–1333. ASME International Mechanical Engineering Congress and Exposition (2009)

Sargusingh, M., Anderson, M., Perry, J., Gatens, R., Broyan, J., Macatangay, A., Schneider, W., Toomarian, N.: NASA Environmental control and life support technology development and maturation for exploration: 2017 to 2018 overview. 48th International Conference on Environmental Systems (2018)

Sunada, E., Bhandari, P., Carroll, B., Hendricks, T., Furst, B., Kempenaar, J., Birur, G., Nagai, H., Daimaru, T., Sakamoto, K., et al.: A two-phase mechanically pumped fluid loop for thermal control of deep space science missions. 46th International Conference on Environmental Systems (2016)

Valdarno, L.: Heat transfer in the porous structure of an additively manufactured evaporator for a two-phase mechanically pumped loop for space applications. University of California, Los Angeles (2022)